Chapter 5

# Nanoscale Insights into Enhanced Raman Spectroscopy

Izabela Rzeznicka and Hideyuki Horino

Additional information is available at the end of the chapter

http://dx.doi.org/10.5772/intechopen.72284

**Abstract**

Enhanced Raman spectroscopies, such as surface-enhanced Raman spectroscopy (SERS) and tip-enhanced Raman spectroscopy (TERS), are based on the amplification of intrinsically weak Raman signals of a molecule by metallic nanostructures. The main enhancement is attributed to electromagnetic enhancement. Chemical effects, such as formation of a surface complex, or a charge-transfer complex, co-adsorbed anion effect, also add to the enhancement of the signal. Using SERS, it has been difficult to study details of chemical enhancement and polarization effects due to limited optical resolution of the technique and usage of roughened metal surfaces. These obstacles were overcome with the development of the TERS technique. TERS has extended Raman spectroscopy into the nanoscale region. In this chapter, nanoscale insights into surface chemistry that lead to Raman signal enhancement are described. The effect of molecular binding and orientation as well as commonly used in SERS chloride activation of metal surfaces is discussed. Finally, we describe the future prospects of TERS and the challenges that keep us from harnessing the full potential of the technique.

**Keywords:** tip-enhanced Raman spectroscopy, surface-enhanced Raman spectroscopy, scanning tunneling microscopy, halogen overlayer, bipyridine, chemical enhancement, molecular orientation, Raman tensor

## 1. Introduction

Raman spectroscopy is an analytical technique based on inelastic scattering of light. The light scattered by a molecule shows a wavenumber shift with respect to the excitation line. This effect was first described by C. V. Raman in 1928 and quickly became used as a powerful method for identifying molecules through their vibrational motions [1]. However, until the 1970s, Raman spectroscopy did not receive much attention of scientists working in the field of surface analysis. This is because intrinsic Raman scattering cross-sections of molecules is small, on the order of $10^{-32}$ cm$^2$ sr$^{-1}$ per molecule [2]. The observation of Raman signal enhancement of

molecules adsorbed on roughened metal surfaces was a corner stone in the development of a family of enhanced vibrational spectroscopies with the surface-enhanced Raman spectroscopy (SERS) being the most widely practiced [3–5]. In SERS, Raman signals are amplified by placing a molecule in the vicinity of metal nanostructures. A large number of papers have been published over a period of 40 years on the origin of Raman signal enhancement on SERS active substrates [6–8]. Consequently, the overall enhancement of the signal has been attributed to two main mechanisms: electromagnetic enhancement (EME) and chemical enhancement (CE).

EME is explained by the enhancement of the electromagnetic field at the molecule's position by excitation of the localized surface plasmon resonances of metallic nanostructures [9, 10]. Basic EME is now well understood and believed to be the major contribution to the enhancement of Raman signals on SERS active substrates. In the process, both the incoming and outgoing field is amplified. For a single molecule, basic EME, excluding polarization effects and tensorial nature of the Raman polarizability, scales as $E^4$, where $E$ is the intensity of the electromagnetic field. Polarization effects influence signal intensity but in a more complex way, depending on the symmetry of the vibrational mode. Moskovits, in his 1982 work, described Raman surface selection rules, that is, modification of band intensities for a molecule adsorbed on a flat metal surface [11]. Experimental justification of polarization effects requires Raman data obtained on flat metal surfaces and a nanoscale characterization of the environment in which a molecule is present. With the development of tip-enhanced Raman spectroscopy (TERS), we can now define the nanoscale environment of a molecule and correlate it directly with the Raman signal. It is expected that polarization studies in TERS settings, supported by calculations of the Raman polarizability tensor components of a molecule, will bring further insights into mechanism of Raman signal enhancement and surface selection rules.

CE describes various effects affecting the Raman polarizability $\alpha^R$ with respect to the $\alpha_0^R$ of a free molecule [12]. Among them is the formation of a metal-molecule complex, anion and field gradient effects [8, 13–16]. CE can be separated into a resonant and nonresonant mechanism. The resonant mechanism is discussed based on the strength of a metal-molecule coupling. In the weak coupling regime, the molecular electronic states may shift and broaden upon their interaction with the metal, and enhancement of the Raman scattering can be achieved by the resonance Raman effect, in which the incident beam is in resonance with the electronic excitation of a molecule. In the strong coupling regime (chemisorption), new electronic states appear, so-called charge-transfer (CT) states that act as intermediate states in Raman scattering [6, 17, 18]. The enhancement of the signal is due to resonance of the incident beam with an excitation from the metal to the molecule or *vice versa*. The nonresonant effect, called the static chemical enhancement, involves various effects, such as the binding geometry of the adsorbate, the influence of co-adsorbed anions and the presence of non-zero static electric fields [14–16, 19, 20]. It has been difficult to investigate how these effects influence the strength of the Raman signals as the signals measured in SERS are averaged over the diffraction-limited spot. A deeper understanding of CE requires Raman studies with nanoscale resolution aided by suitable electronic structure calculations of the molecule-metal system.

Combining Raman spectroscopy with scanning probe microscopy into so-called TERS has made it possible to investigate CE and EME in detail with nanoscale resolution [21, 22]. TERS is an offspring of SERS, in which a "hot spot" is created between a metallic tip and a flat surface.

The TERS technique eliminates the need for rough or nanostructured surfaces, allowing for investigation of the details of molecular adsorption under well-defined conditions. The biggest advantage of TERS over SERS is its capability to acquire Raman signals and nanoscale images of the molecule adsorbed on a solid substrate simultaneously.

In this chapter, readers will be introduced to the experimental and theoretical aspects of TERS based on a scanning-tunneling microscopy (STM-TERS). Subsequently, the results of TERS studies of molecules adsorbed on flat metal surfaces are summarized with an emphasis on the molecular orientation and surface selection rules. Later, the effect of chlorine activation of metal surfaces on the adsorption of organic molecules and halogen overlayer-templated growth of surface-grown metal-organic layered structures are described. At the end of the chapter, future prospects and challenges of TERS in studies of molecular adsorption on metal surfaces are discussed.

## 2. Tip-enhanced Raman spectroscopy

### 2.1. TERS technique: a historical overview

Nanoscale vibrational spectroscopy has been a longstanding dream of scientists working in various fields. In the early 1980s, a scanning tunneling microscope was invented which brought us the capability to explore surfaces with unprecedented subnanometer scale resolution [23]. Later on, images of molecules adsorbed on metal and semiconductor surfaces were obtained [24]. STM is based on a tunneling current between a conductive surface and a sharp metallic tip. In the basic mode of operation, STM does not yield vital chemical information, and formation of surface complexes cannot be confirmed. Consequently, inelastic electron tunneling spectroscopy (IETS) was developed to obtain chemical information from single molecules adsorbed on metal surfaces [25]. Despite its ultimate resolution and sensitivity, IETS has not evolved into a common nanoscale vibrational spectroscopic method. This is because IETS is a very challenging technique requiring low temperature, ultra-high vacuum conditions and ultra-low noise electronics.

From the development of the field of plasmonics and the demonstration of large electromagnetic field enhancement in SERS experiments, the idea of nanoscale vibrational spectroscopy on surfaces using Raman scattering has been brought to life [26]. Raman spectroscopy has many advantages as it is based on the optical response of the system and can be applied under ambient conditions and in water. However, Raman scattering is intrinsically a very weak process with only one in every $10^6$–$10^8$ incident photons being scattered [27]. Theoretical reports in the late 1990s showed that the electric field at the metallic tip end is dramatically enhanced under certain polarization direction [28]. This report inspired scientists working in the field of optical microscopy and surface science to utilize the enhancement effect to develop a high-resolution molecular spectroscopic technique. The Kawata group in Japan and the Zenobi group in Switzerland simultaneously reported TER spectra from multilayers of organic molecules deposited on a glass surface using a metalized cantilever probe of an atomic force microscope (AFM) [21, 22]. Later, Pettinger *et al.* reported TER spectra from the monolayer of malachite green adsorbed on $CN^-$ modified gold surface, using STM tip [29]. Ultimate

sensitivity and resolution of a single molecule were demonstrated in 2008 with TERS optics incorporated into ultra-high vacuum environment (UHV-TERS) [30]. Over the last decade, TERS has been adapted as an analytical tool in chemistry, biology and materials science [31].

## 2.2. Experimental aspects of STM-TERS

### *2.2.1. Tip fabrication and related issues*

A sharp metallic tip is a central part of the TERS setup and its quality (size and shape) defines the spatial resolution of TERS and, to some extent, the magnitude of the enhanced field. Owing to its importance, several papers have discussed various tip fabrication methods [32–34]. Tips are usually made of gold or silver as these metals have plasmon resonances in the visible region of the electromagnetic spectrum. Electrochemical etching is a common method to prepare the tips. In a typical procedure, Au tips are prepared by direct current electrochemical etching in a 50:50 (v:v) mixture of concentrated HCl and ethanol. Au wire (a tip after etching) serves as the anode and a gold or platinum ring acts as the cathode. The end of the Au wire is submerged 1–2 mm into the solution at the center of the gold ring. A voltage in the range of 1.7–2.5 V is applied between the cathode and the anode. The etching reaction proceeds until the electrochemical current drops to zero. Typically tips with a tip-apex size in the range of 20–50 nm are obtained in this way.

### *2.2.2. Optical geometries*

TERS requires integration of STM/AFM with the optical components used in Raman spectroscopy. Various optical geometries have been adapted in the past 15 years to work with a variety of different samples [34]. They include a bottom-, side-, top- and a parabolic mirror illumination depicted in **Figure 1**. Each geometry has its own advantages and disadvantages, which are summarized hereafter.

The bottom illumination geometry (**Figure 1a**), in which the incident laser light is fed through the microscope objective placed at the bottom and the rear side of the sample, is not practiced among STM-based TERS users as it requires transparent samples. This geometry is commonly used in AFM-based TERS, in which an inverted optical microscope platform is used. The advantage of this geometry is a very high collection efficiency of scattered light as oil-immersion objectives with a high numerical aperture (NA) can be used. Recently, the Deckert group has modified the bottom illumination geometry to work with opaque samples by using

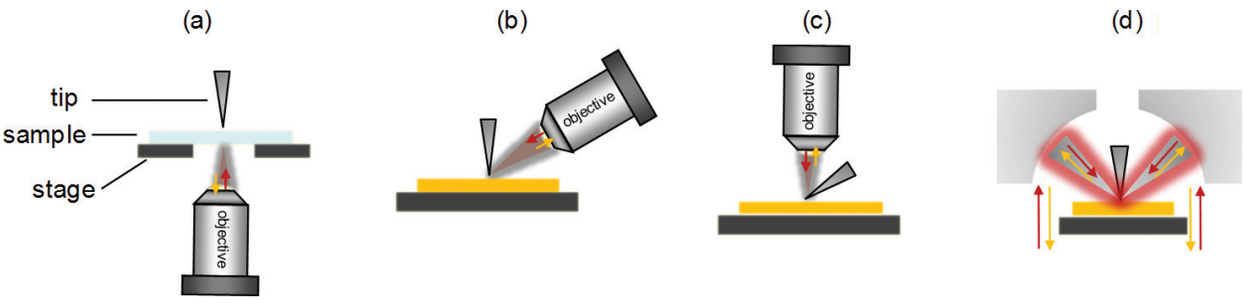


**Figure 1.** Four common optical geometries used in TERS (a) bottom illumination, (b) side illumination, (c) top illumination, (d) parabolic mirror illumination.

a dichroic mirror and passing the incident light through the transparent side of the opaque sample [35]. The bottom illumination is well suited for biological samples.

Side illumination (**Figure 1b**) is the most commonly used setup in TERS built on STM. In this geometry, the incoming laser light as well as the outgoing scatter signal is collected by a long working distance microscope objective placed at an angle in the range of 45–70° relative to the tip axis that maximizes the electric light component along the tip axis. The advantage of this geometry is an easy integration with commercial STM setups. It can be used both for transparent and nontransparent samples. However, only conductive samples can be studied. The disadvantage of the side illumination geometry is relatively low collection efficiency in comparison to the bottom light illumination geometry. This is because objective lenses with a low numerical aperture are employed due to space restriction around the STM tip. Another disadvantage of the side illumination geometry is an asymmetric illumination of the tip, which leads to larger spot size and higher far-field background. In addition to tip resonances, so-called gap mode resonances can be excited in the side illumination geometry [36, 37]. They play a big role in the enhancement of the signal when the distance of the tip to the surface is below 2 nm [38]. Excitation of the gap-mode resonances improves sensitivity and resolution of the TERS technique. The side illumination geometry is widely used in the field of surface science.

Top illumination (**Figure 1c**) is the second most commonly used geometry in the STM-TERS community. This geometry makes focusing of the incident beam on the STM tip easier. The tip is placed at an angle to the surface with the microscope objective placed normal to the surface. Although some of the scattered light is shadowed by the tip, this geometry offers still higher excitation and collection efficiency than the side-illumination geometry does. Another advantage is a reduction in the far-field background. Both opaque and transparent samples can be studied. This geometry is ideally suited for investigating nanoscale phenomena on silicon or graphene samples.

A geometry utilizing a parabolic mirror (**Figure 1d**) was first demonstrated by researchers working with an STM unit operating in UHV conditions [30]. It was developed in order to increase the collection efficiency by allowing collection of light from all directions. In this geometry, a hole is made in a parabolic mirror to accommodate the STM tip. STM-TERS setups with a parabolic mirror work in a reflection mode, allowing both opaque and transparent samples to be studied. Compared to the side and top illumination geometries, the parabolic mirror geometry offers high collection efficiency. Two major disadvantages of this geometry are: it is difficult to integrate into commercial STM units and optical alignment is difficult. A small angular mismatch results in defocusing of the laser spot and loss of the signal. Thus, this geometry has not been widely used.

### 2.3. Understanding TERS

The origin of Raman signal enhancement in TERS is similar to that in SERS, which is due to EME and CE. In contrast to SERS, in which Raman signals are obtained from multiple hot spots across the surface, the signal in TERS originates from one central hot spot, which is created between the apex of a tip and a flat metal substrate.

Various effects, such as electrostatic lightening rod effect, excitation of localized surface plasmon polaritons (SPPs) on the tip and antenna resonances, contribute to EM field enhancement [39]. The lightening rod effect is independent of the excitation wavelength. On the other hand,

excitation of SPPs is wavelength dependent with maximum field enhancement achieved when the laser energy coincides with the localized surface plasmon resonances of the tip. Finite-difference time domain (FDTD) calculations show that the magnitude of the enhancement due to plasmon excitation depends on the laser light polarization, tip radius and dielectric properties of the surrounding medium [38]. In-plane light polarization (*p*-polarization, parallel to the tip axis) gives much higher enhancement than the out-of-plane polarization (*s*-polarization) does. The maximum enhancement is predicted for tips with the apex radius of 15–20 nm [38]. Tips made of silver provide higher enhancement when visible light excitation is used. **Figure 2** shows all possible effects contributing to the enhancement of the signal in TERS.

When the tip-metal surface distance is smaller than 2 nm, additional EM field enhancement is observed. At this distance, LSP of the tip and a metal interact with each other to form hybridized modes, called gap modes [37]. The enhancement due to excitation of the gap mode resonances depends strictly on the tip-metal surface separation [40, 41]. The gap modes are efficiently excited when $D/R < 1$, where $D$ is the distance of the particle from the surface and $R$ is the radii of the tip apex. The enhancement of the scattered light intensity is found to be as high as $10^{12}$ for a 20 nm radius gold tip and tip-substrate separation of 1 nm [38]. Such small tip-substrate separations are easily controlled by the tunneling feedback function of the STM.

CE due to chemisorption, formation of a surface-complex and anion surface modification can be studied with excellent resolution using STM-TERS. These studies began in the field of surface science. A resonance enhancement of $10^6$ has been reported by Pettinger *et al.* for a malachite green molecule adsorbed on an Au(111) surface [42]. Ren *et al.* have shown that Raman signal can be obtained from monolayers of non-resonant molecules with weak Raman cross-sections [43]. Observed frequency shifts between Au and Pt surfaces indicate that TERS is sensitive enough to identify molecular orientation and revealed details of molecule-surface interaction.

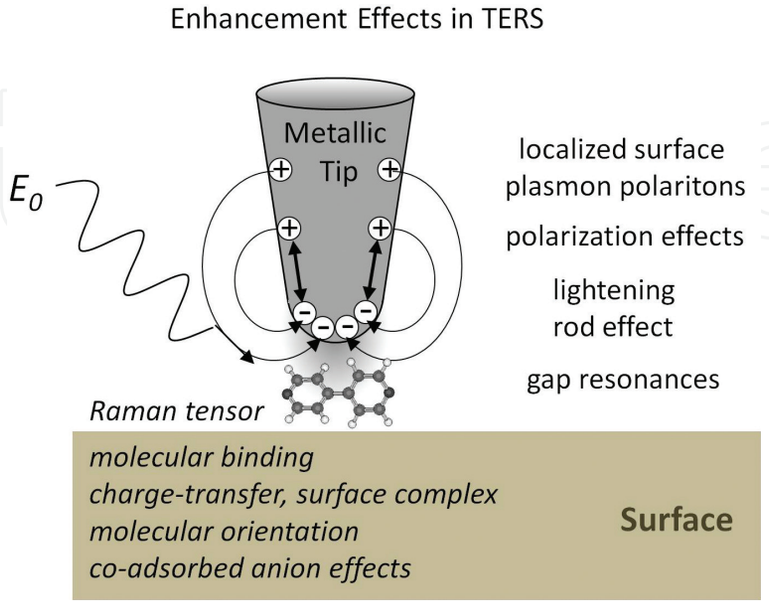


**Figure 2.** Possible CE and EME effects contributing to Raman signal enhancement in TERS.

Although simultaneous observation of Raman and infrared (IR) vibrational modes are exclusive to each other in the case of centrosymmetric molecules, some TER spectra published in the literature show the presence of IR active or silent modes [44]. Polbutko explained appearance of these lines due to strong quadrupole light-molecule interactions arising from strongly inhomogeneous electromagnetic fields, which exist near rough metal surface [45].

The Dong group has recently demonstrated sub-nanometer resolution in TERS experiments [46]. As subnanometer resolution is difficult to understand in terms of the classical electromagnetic theory, these results have inspired theoreticians to work on proposing new mechanisms that could explain the results. Duan and Luo have proposed involvement of nonlinear optical processes [47]. Creation of an "atomic-scale hot spot" has also been proposed [48]. In addition, multiple elastic scattering of light between molecular dipoles adsorbed on the surface has been proposed to explain the improved signal intensity and TERS spatial resolution [49].

The ultimate goal to understand TERS from molecules adsorbed on metal surfaces is to understand how relative intensities of Raman lines depend on the molecular orientation and polarization direction of the excitation light. These studies are still challenging as there are many parameters, such as molecular binding geometry, Raman tensors and direction of local field polarization, that have to be determined. It is still not possible to formulate rules similar to the IR metal surface-selection rule (SSR). The IR SSR states that, for a molecule adsorbed on a metal surface, vibrational modes having a dipole moment perpendicular to the surface are the most enhanced [50]. Moskovits described the concept of SSR in SERS experiments for flat metal surfaces [11]. The author's work in 1982 gave theoretical grounds for local field polarization. Recently, Ru *et al*. have experimentally validated Moskovits theory by studying polarization and incident angle dependences of the SERS signals [51]. Similar studies using TERS can offer more insights into the Raman SSR as the Raman signal can be directly related to the molecules present under the tip.

In order to comprehend enhancement mechanisms in detail, more sophisticated experiments and theoretical analysis are required. Emerging TERS studies under UHV and on well-defined systems can deliver more results, which should eventually bring us closer to understanding origin of signal enhancement and contribute to the development of TERS as a reliable analytical tool.

## 3. Enhancement of Raman signals due to chemisorption

This section summarizes our studies on molecular adsorption and orientation of 4,4′-bipyridine (4,4′-BiPy) and 4,4′-bipyridine *N,N*′-dioxide (4,4′-$BiPyO_2$) in monolayers formed on gold thin films deposited on muscovite mica substrates using STM-TERS supported by calculated Raman tensor polarizability components. The enhancement of the Raman signals is attributed to the formation of a chemisorbed overlayer with a standing up molecular configuration [52].

### 3.1. Experimental details

A TERS setup with the side-illumination geometry was used in the experiments described here. The setup consists of a commercial STM unit (Nanoscope E, Veeco Instruments Inc., USA), a spectrograph (SP-2150i, Roper Scientific, GmbH) and optical components. The STM

has a modified piezo scanner head which allows to install a high numerical aperture objective lens (Mitutoyo, LWD 100×, NA = 0.7, WD = 6 mm) in front of the STM tip. The lens is placed at an angle of 60° to the surface normal with the light polarization parallel to the tip axis (*p*-polarization). This objective lens is used to deliver the excitation laser beam as well as to collect the backscattered light from a tip-surface junction.

The optical pathway adapted in the study is shown in **Figure 3**. A red, He-Ne laser beam (632.8 nm, max. Output 30 mW, CVI Melles Griot, USA) with circular polarization was used for the excitation. The laser light was allowed to pass through a band-pass filter (Sigma Koki, Japan, bandwidth = 3 nm) and a polarizer. A transmitted light was reflected by a mirror, passed through a 45° dichroic beam splitter (RazorEdge, type U, Semrock), and reflected by two other mirrors before being focused on the tip-surface junction by the objective lens.

The backscattered radiation is collected by the same objective lens and reflected by two mirrors before falling on the dichroic beam splitter. The scattered signal passes through an ultra-steep long-pass edge filter (RazorEdge, type E, Semrock), and is focused by a lens (diameter = 25 mm, focal length = 100 mm) onto the slit of the spectrograph. A back-illuminated, charge-coupled device (CCD) camera (Spec-10, Princeton Instruments) cooled by liquid nitrogen was used to acquire Raman spectra. The spectrograph was installed with 300 g/mm diffraction grating. The spectral resolution of the system was 10 $cm^{-1}$. All experiments were carried out in ambient conditions with the incident laser power of 0.4 mW, giving power density of $8 \times 10^7$ $W/m^2$ in the focal region.

### 3.2. Details of theoretical calculations used to derive molecular orientation

The geometry of the molecules and fundamental vibrational frequencies were calculated using the Gaussian 09 package. Molecular structures in the ground state were optimized by the B3LYP exchange-functional of the density functional theory and 6-31G++(d,p) basis set [53]. The optimized geometries of both molecules (4,4′-BiPy and 4,4′-$BiPyO_2$) are nonplanar

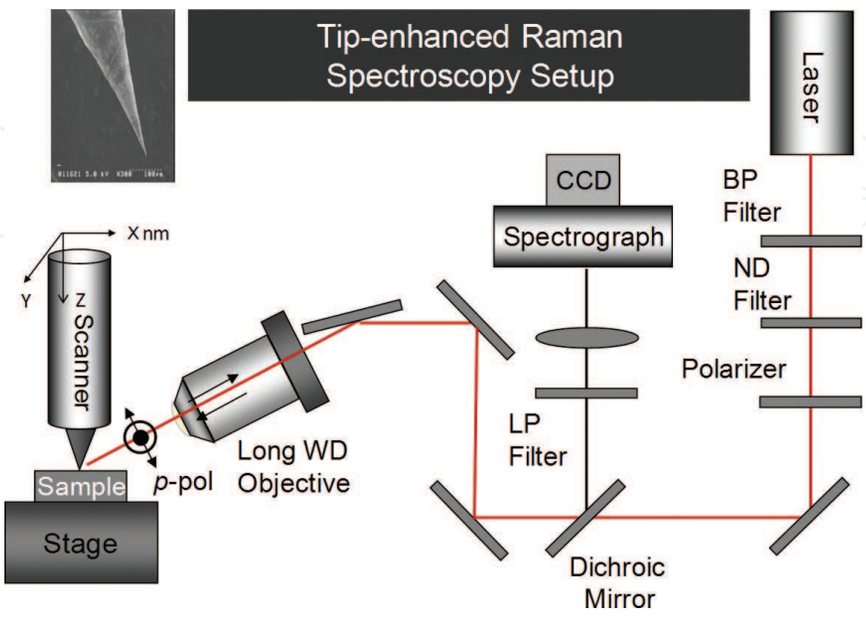


**Figure 3.** STM-TERS setup. The inset shows a SEM picture of the Au tip, etched at a bias of 2.4 V. Adapted from Rzeznicka *et al.* [52]. Copyright@Elsevier B.V.

with $D_2$ symmetry. Each vibrational mode has been ascribed to a given symmetry mode and Raman polarizability tensor components were calculated for each of the mode.

The intensities of the Raman scattering were evaluated with the matrix elements of the Raman tensor, $\langle k \mid \hat{\alpha}_{ij} \mid 0 \rangle$, where $\hat{\alpha}_{ij}$ $(i, j = x, y, z)$ denotes the polarizability tensor in usual (electronic off-resonant) conditions, and $|0\rangle$ and $|k\rangle$ are the vibrational ground state and the first excited state for the normal mode $k$ (= 1, 2,…, 3$n$−6), respectively [54]. This matrix element is represented in the harmonic approximation with the polarizability derivative with respect to the normal mode coordinate $Q_k$ as follows:

$$\langle k \mid \hat{\alpha}_{ij} \mid 0 \rangle = \sqrt{\frac{\hbar}{2\mu_k \omega_k}} \frac{\partial \alpha_{ij}}{\partial Q_k} \tag{1}$$

where $\hbar$ is the Planck constant divided by 2π, $\omega_k$ and $\mu_k$ are the angular frequency and the reduced mass of the mode $k$, respectively. The molecule-fixed coordinates were defined with the principal axes of inertia, where the $z$ axis is along the long molecular axis, and the $x$ axis is nearly perpendicular to the rings. The principal axes of polarizability tensor coincide with the $x$, $y$ *and* $z$ axes, to give $\alpha_{xx}$, $\alpha_{yy}$ and $\alpha_{zz}$. The vibrational analysis was performed to obtain the frequency $\omega_k$, normal mode coordinate $Q_k$ and the reduced mass $\mu_k$ of each mode $k$. The polarizability tensor components, $\alpha_{ij}$, were calculated by the facilities involved in Gaussian 09 with varying molecular geometries displaced along the normal coordinate $Q_k$, and the derivatives $\partial \alpha_{ij}/\partial Q_k$ were obtained by five-point numerical differentiation of the calculated polarizability tensor. The Raman tensor elements, $\langle k \mid \hat{\alpha}_{ij} \mid 0 \rangle$, in Eq. (1) were derived in this way. Subsequently, Raman scattering intensity was simulated. The intensity of the light scattered from the molecule is proportional to the square of the electric vector of the Raman scattered light, $E_{sc}$, which is related to the electric vector of the incident light, $E_0$ through the characteristic molecular Raman tensor, $(\alpha_{ij})$ $(i, j = x, y, z)$

$$\left|E_{sc}\right| \propto \left|\left(\alpha_{ij}\right)E_0\right| \tag{2}$$

In order to determine orientation of the molecule, the experimental scattering intensities were compared with the scattering intensities calculated for three representative molecular orientations. The direction of the incident radiation was described in the surface-fixed coordinate system ($X$, $Y$, $Z$). The polarization of an incident laser beam in our TERS experiment was adjusted in a way that the electric vector, $E_0//Z$, that is, $Z$ axis is perpendicular to the surface. The molecules can take various orientations having various molecular Euler angles, with respect to the Au substrate plane. Three representative configurations were considered, that is, when $x//Z$, $y//Z$ and $z//Z$. The corresponding molecular orientation for each case is shown in **Figure 4**. For the molecule perpendicular to the surface ("end-on" configuration), the molecular $z$ axis is parallel to the surface-fixed $Z$ axis ($z//Z$), that is, perpendicular to the surface. The molecule with the "edge-on" configuration and the "face-on" configuration are denoted as $y//Z$ and $x//Z$, respectively.

### 3.3. Adsorption and molecular orientation of 4,4′-BiPy on Au(111)

Adsorption of 4,4′-BiPy on the surface of an Au thin film proceeded in two stages. A first adsorption stage was observed after a short immersion time (3–5 h) of the Au film into a 1 mM ethanolic solution of 4,4′-BiPy. An image of the surface at this stage is shown in **Figure 5a**. No well-defined

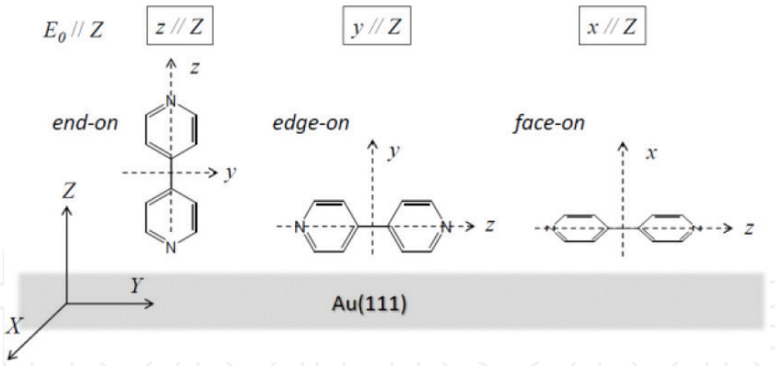


**Figure 4.** Molecular coordinate system. The molecular axes are x, y and z, and the surface axes are X, Y and Z. The three cases of adsorption configuration discussed in the text are shown. *E* defines the electric vector of an incident radiation. Adapted from Rzeznicka *et al*. [52]. Copyright@Elsevier B.V.

overlayers were observed. The surface of Au looked very rough and dynamic. Imaging was very unstable due to apparent adsorbate-induced surface reconstruction. Surface reconstruction is associated with the ejection of gold atoms and their diffusion over the surface. Low-coordinated gold atoms are highly reactive, and they may form a complex with molecules in the solution and diffuse over the surface to stable adsorption sites. These transient species are seen in the image as whitish spots. A second stage of adsorption was observed upon a prolonged immersion time. In this stage, a well-defined overlayer was formed. An STM image of the surface immersed into

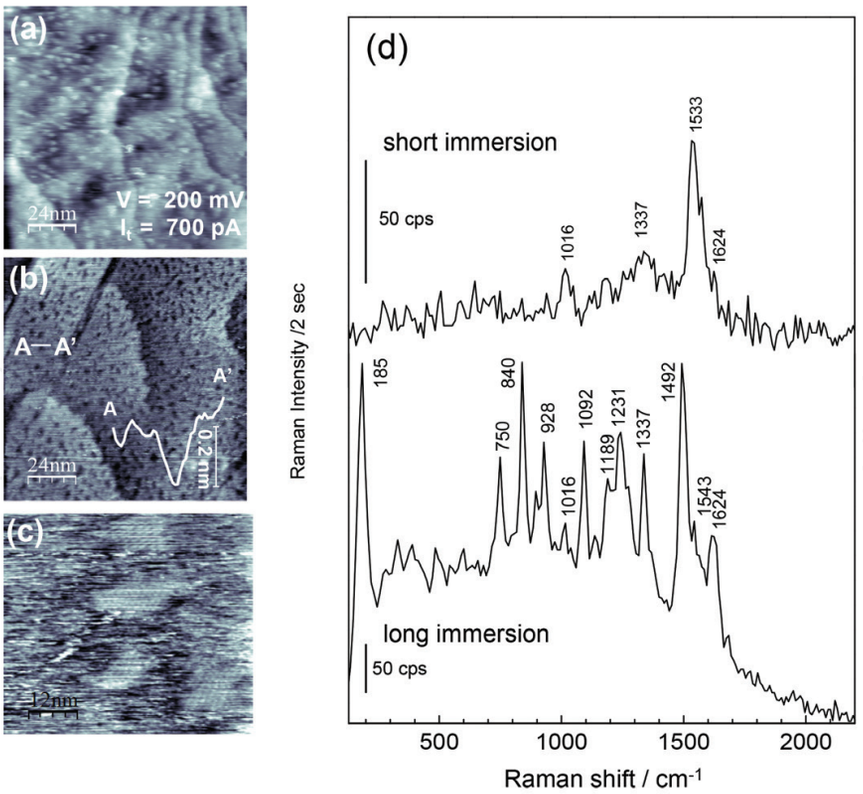


**Figure 5.** STM images of 4,4-BiPy adlayer formed on Au(111) after immersion of the film into a 1 mM ethanolic solution for (a) 3 hours, (b) 4 days and (c) zoom into (b). (d) TERS spectra corresponding to the layer shown in image a and b. A depth profile across the A-A' line is shown in image (b). Adapted from Rzeznicka *et al*. [52]. Copyright@Elsevier B.V.

the solution for 4 days is shown in **Figure 5b**, **c**. A homogeneous monolayer with pits having a depth of a single-gold-atom was observed. It looks similar to monolayers formed by alkanethiols on Au surface, indicating involvement of Au adatoms in the process of self-assembly. TER spectra for the short immersion time and the long immersion time are shown in **Figure 5d**. The Raman spectrum for the short immersion time has only few bands with very low intensity. The absence of low-frequency vibrational signals, which could be assigned to Au-N stretching band, indicated that molecules were only weakly adsorbed (physisorbed) on the surface. In the case of the long immersion time, intensities of the Raman signals were higher, and many vibrational bands, which were not observed in the case of the short immersion time, appeared. An intense Au-N stretching signal was detected at 185 $cm^{-1}$, indicating that molecules were chemisorbed on the surface.

Vibrational frequencies for the two cases are summarized in **Table 1**. Each mode has been ascribed to a given symmetry mode, and Raman polarizability tensor components were calculated for each of the mode. The scattering intensities for the three possible molecular orientations were calculated and used to aid in determining the molecular orientation.

First molecular orientation of 4,4′-BiPy in the case of long immersion time is discussed.

| **Experimental TERS peak position/$cm^{-1}$** | | **Results of calculations** | | | | | | **Modal assignment** |
|---|---|---|---|---|---|---|---|---|
| **Figure 5** | **Figure 5** | | | | **$\|(\alpha_{ij})E_0\|(\|E_0\| = 1)$/ atomic unit** | | | |
| **Short immersion** | **Long immersion** | **Frequency /$cm^{-1}$** | **Symmetry class** | **Mode number *k*** | ***x*//*Z*** | ***y*//*Z*** | ***z*//*Z*** | |
| | 185 *s* | — | — | — | — | — | — | ν(Au-N) |
| | 750 *m* | 688 | $B_2$ | 13 | 0.25 | 0 | 0.25 | pyridyl ring deformation |
| | 840 *s* | 864 | $B_2$ | 18 | 0.26 | 0 | 0.26 | γ(C–H) + γ(C–C) + γ(C–C)int + γ(C-N) |
| | 928 *m* | 984 | $B_2$ | 22 | 0.01 | 0 | 0.01 | γ(C-H) |
| 1016 *w* | 1016 *w* | 1014 | *A* | 26 | 0.44 | 0.73 | 1.94 | γ(C-H) + δ(C-C) + δ(C-N) + ν(C-C) + ν(C-N) |
| | 1092 *m* | 1098 | *A* | 29 | 0.15 | 0.11 | 0.52 | δ(C-H) + δ(C-C) + δ(C-N) + ν(C-N) |
| | 1231 *m* | 1276 | $B_2$ | 34 | 0.16 | 0 | 0.16 | ν(C-C) + ν(C-N) |
| 1337 *m* | 1337 *m* | 1364 | $B_3$ | 38 | 0 | 0.32 | 0.32 | δ(C-H) + ν(C-C) |
| 1533 *s* | 1492 *s* | 1540 | *A* | 42 | 0.14 | 0.47 | 0.88 | δ(C-H) + ν(C-C) + ν(C-C)int + ν(C-N) |
| | 1543 *m* | 1583 | $B_2$ | 43 | 0.07 | 0 | 0.07 | δ(C-H) + ν(C-C) + ν(C-N) |
| 1624 *w* | 1624 *m* | 1645 | *A* | 46 | 0.22 | 0.83 | 3.43 | δ(C-H) + ν(C-C) + ν(C-C)int + ν(C-N) |

*s*-strong, *m*-medium, *w*-weak intensity.

The symmetry index stands on $D_2$ class for a free molecule.

ν-stretching; δ-in-plane bending; γ-out-of-plane bending; ν(C-C)int denotes interring C-C vibration.

Adapted from Rzeznicka *et al.* [52]. Copyright@Elsevier B.V.

**Table 1.** Experimental and calculated Raman scattering data for 4,4′-BiPy.

As expected for the polarization direction perpendicular to the surface only vibrational modes with $A$, $B_2$ ($xz$) and $B_3$ ($yz$) symmetry are observed. For the observed vibrational modes, only the "end-on" orientation does not have null Raman intensity values suggesting that the "end-on" orientation is the most plausible. The values are equally distributed over all symmetry modes, which imply that the molecule is tilted in all three directions of Au(111) surface. A presence of the Au-N stretching peak is another strong evidence to support the "end-on" orientation 4,4′-BiPy. Henceforward, we concluded that the 4,4′-BiPy molecules, in the case of long immersion time are adsorbed in a standing-up but tilted orientation, with one of two nitrogen ends anchored to Au.

In the case of short immersion time, many of the vibrational peaks seen in the long immersion time spectrum were missing. There was no Au-N stretching signal, and the $B_2$-symmetry vibrational modes were not observed which rejects possibility of the "face-on" configuration. The peak intensities coincide with the y//Z-values of $|(\alpha_{ij})E_0|(|E_0| = 1)$ in **Table 1**. For the missing signals, the calculated y//Z-value of $|(\alpha_{ij})E_0|(|E_0| = 1)$ is zero or nearly zero. Henceforward, we concluded the 4,4′-BiPy has y//Z orientation, that is, the "edge-on" orientation, without the N atoms bonded to the Au substrate.

Our analysis is based on Raman polarizability tensor components calculated for a free molecule and on the assumption that a local electric field is perpendicular to the surface. As in the case of long immersion, chemisorption may change polarizability of the bonds, and Raman tensor elements may be different than the tensor elements calculated for a free molecule.

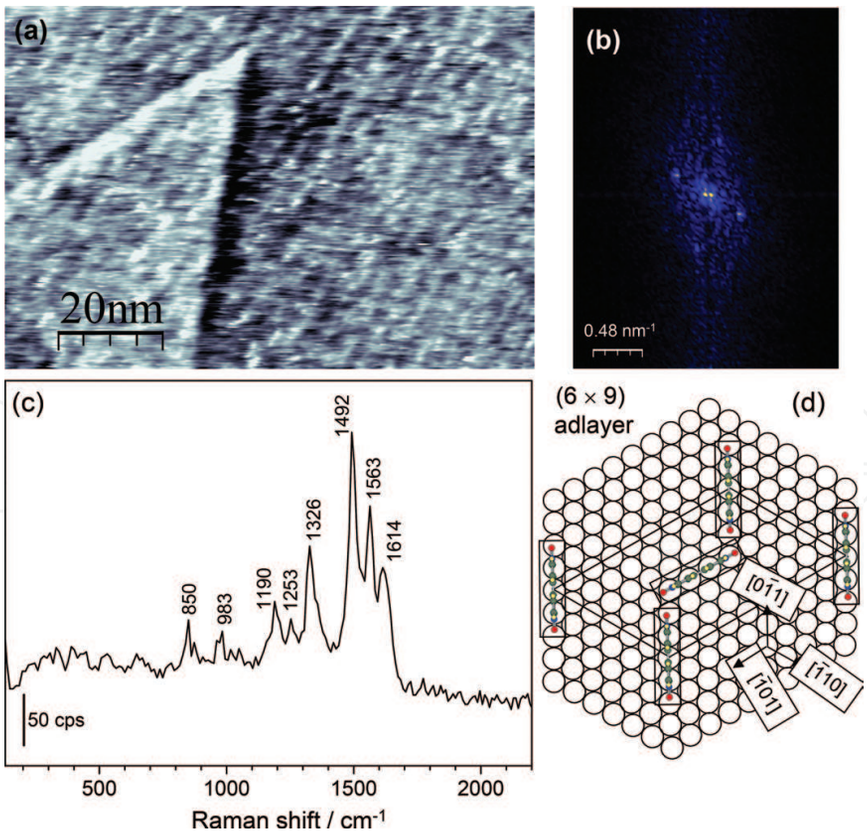


**Figure 6.** (a) 100 × 70 nm constant current STM image of 4,4-BiPyO$_2$ adlayer formed on Au(111) after immersion of the film in a neutral, 1 mM ethanolic solution for 6 h. (b) the two-dimensional Fourier-transform of the image. (c) TERS spectra of the overlayer. (d) Schematic representation of a (6 × 9) BiPyO$_2$ adlayer. Adapted from Rzeznicka *et al.* [52]. Copyright@Elsevier B.V.

### 3.4. Adsorption and molecular orientation of 4,4′-$BiPyO_2$ on Au(111)

**Figure 6a** shows an STM image of the Au surface upon 30 min immersion into a neutral 1 mM ethanolic solution of 4,4′-$BiPyO_2$. A two-dimensional overlayer, consisting of parallel rows, extending over a triangular terrace of the Au(111) surface was observed. A two-dimensional Fourier transform (2D–FFT) of the image, shown in **Figure 6b**, revealed the spacing between parallel rows to be 1.5 and 2.2 $nm^{-1}$, respectively. The angle between stripes and the edges of the terrace was 30°. The overlayer is designated as (6 × 9) overlayer. **Figure 6c** shows TER signals from an Au thin film surface immersed for 6 h in a neutral 1 mM ethanolic solution of 4,4′-$BiPyO_2$. The spectrum contains a peak at 850 $cm^{-1}$, assigned to the in-plane ring vibrations and the N-O stretching vibrations, and a peak at 1190 $cm^{-1}$, which draws its intensity mainly from the in-plane C-H bending vibrations. The position of these bands falls into the frequency region of the uncoordinated 4,4′-$BiPyO_2$. The most intense band is at 1492 $cm^{-1}$ followed by peaks at 1563 and 1614 $cm^{-1}$, similarly to 4,4′-BiPy. No Au-N or Au-O stretching bands were found in TER spectrum, which indicated rather weak interaction of 4,4′-$BiPyO_2$ with the Au substrate. Orientation of the 4,4′-$BiPyO_2$ is deduced in the same manner, as done for 4,4′-BiPy.

Vibrational frequencies, their symmetry modes and calculated Raman intensities are summarized in **Table 2**. TER spectrum for 4,4-$BiPyO_2$, shown in **Figure 6c** contains three bands in A symmetry. Since neither Au-O nor Au-N vibrational modes were observed, it is more likely that a molecule has its molecular long axis parallel to the Au surface.

In **Table 2**, x//Z-values of $|(\alpha_{ij})E_0|(|E_0| = 1)$ do not follow the real spectral intensity. The calculated x//Z-values are zero for the $B_3$ bands. On the other hand, the values for y//Z and z//Z

| **Experimental TERS peak position/$cm^{-1}$** | | **Results of calculations** | | | | | | **Modal assignment** |
|---|---|---|---|---|---|---|---|---|
| **Figure 6** | | | | | **$\|(\alpha_{ij})E_0\|(\|E_0\| = 1)$/ atomic unit** | | | |
| **TERS** | **Powder Raman** | **Frequency/ $cm^{-1}$** | **Symmetry class** | **Mode number *k*** | ***x*//*Z*** | ***y*//*Z*** | ***z*//*Z*** | |
| 850 *w* | 852 *m* | 858 | $B_1$ | 24 | 0.22 | 0.22 | 0 | δ(C-H) + δ(C-C) + ν(C-N) + ν(N-O) |
| 1190 *m* | 1202 *m* | 1210 | *A* | 37 | 0.10 | 0.63 | 3.55 | δ(C-H) |
| 1253 *w* | | 1266 | $B_3$ | 39 | 0 | 0.51 | 0.51 | ν(C-C) + ν(C-N) |
| 1326 *m* | 1300 *m* | 1319 | *A* | 40 | 0.23 | 0.51 | 7.16 | δ(C-H) + δ(C-C) + δ(C-N) + ν(C-C) + ν(C-C)int |
| 1492 *s* | 1512 *m* | 1499 | $B_3$ | 46 | 0 | 0.23 | 0.23 | δ(C-H) + ν(C-C) |
| 1563 *s* | | 1572 | $B_3$ | 50 | 0 | 0.39 | 0.39 | δ(C-H) + ν(C-C) + ν(C-N) |
| 1614 *m* | 1617 *s* | 1667 | *A* | 51 | 0.27 | 0.92 | 9.67 | δ(C-H) + δ(C-C) + δ(C-N) + ν(C-C) + ν(C-C)int + ν(C-N) + ν(N-O) |

*s*-strong, *m*-medium, *w*-weak intensity.

The symmetry index stands on $D_2$ class for a free molecule.

ν-stretching; δ-in-plane bending; γ-out-of-plane bending; ν(C-C)int denotes interring C-C vibration.

Adapted from Rzeznicka *et al.* [52].Copyright@Elsevier B.V.

**Table 2.** Experimental and calculated Raman scattering data for 4,4′-$BiPyO_2$.

follow the observed frequencies, except for the peak at 850 $cm^{-1}$. The value of $|(\alpha_{ij})E_0|(|E_0| = 1)$ is zero for z//Z. The appearance of this 850 $cm^{-1}$ band denies z//Z orientation. In conclusion, the Raman signal intensity supports the "edge-on" orientation.

## 4. Enhancement of Raman signals due to halogen overlayer-templated crystal growth

This section describes particular surface chemistry leading to the growth of metal-organic surface crystals in the presence of halogen overlayer. The crystals were grown on an Au surface from ethanolic solutions of 4,4′-BiPy, in the presence of HCl. STM-TERS and ordinary Raman spectroscopy were used to reveal details of a crystal growth [55].

### 4.1. Chlorine overlayer-templated growth of Au-4,4′-BiPy crystals on Au(111)

**Figure 7a** shows a large area STM image of the Au surface obtained after immersion of Au/mica film into a 4,4′-BiPy solution, adjusted with 0.1 M HCl to pH 3, for 2 days at room temperature. A zoom into the flat part of the image shows a periodic overlayer structure, shown in **Figure 7b**. The overlayer consists of bright stripes having a width of ~7.5 Å. The width is close to the length of 4,4-BiPy, which measures ~ 7.1 Å. Each stripe shows contrast modulation with periodicity of

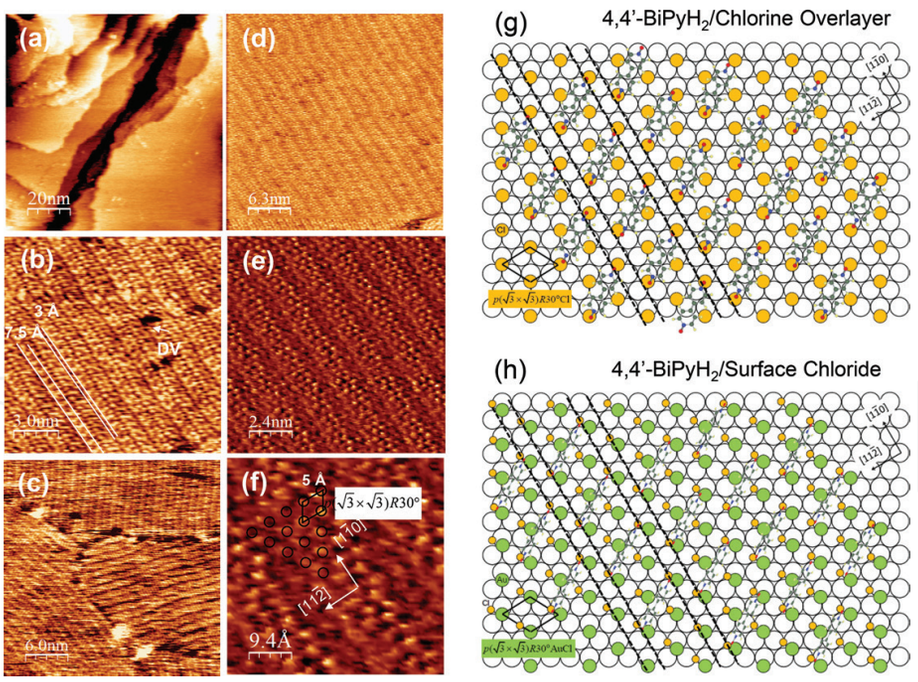


**Figure 7.** STM images after immersion of Au slide into 1 mM ethanolic solution of 4,4-BiPy, acidified to pH = 3 with HCl: (a) 100 × 100 nm image showing well-defined overlayer; (b) 15 × 15 nm zoomed image into (a) showing a striped structure; (c) 30 × 30 nm image showing rotational domains; (d) 31 × 31 nm image showing a p($\sqrt{3}$ × $\sqrt{3}$)R30°-Cl overlayer structure; (e) zoomed 12 × 12 nm image of (d); (f) zoomed 4.7 × 4.7 nm image of (e) into the p($\sqrt{3}$ × $\sqrt{3}$)R30°-Cl overlayer. Possible molecular models of the striped structure; (g) growing on top of chlorine overlayer and (h) growing on top of surface chloride. Adapted from Rzeznicka *et al.* Copyright@Elsevier B.V [55].

~ 3 Å, as indicated in the figure. The overlayer has few dark vacancies (DV). The depth of dark vacancies is in the range of 1.3–1.5 Å. The overlayer was observed to grow along the crystallographic directions of the underlying Au(111) surface as shown in **Figure 7c**. By careful alternation of the tunneling current and scanning speed, another structure originated from the underlying layer was detected, as shown in **Figure 7d** (notice the transition at the bottom of the image). In this underlying layer, individual atoms are found to be arranged in a rectangular lattice with a unit cell of $a$ = 5 Å. **Figure 7(e**, **f)** shows large area and a zoom image of the lattice. This atomic arrangement is assigned to the $p(\sqrt{3} \times \sqrt{3})R\,30^{\circ}$ structure, which has been observed upon adsorption of 0.33 ML of $Cl_2$ onto the Au(111) surface at room temperature [56]. The density functional theory (DFT) calculations predicted that the fcc hollow site is the most stable adsorption site for chlorine in this overlayer [56]. Based on these facts, the most possible molecular model for the stripe phase observed after adsorption of 4,4′-BiPy onto the Au(111) surface in the presence of chlorine ions was proposed. The proposed overlayer structure is shown in **Figure 7g**. In this model, $[4,4'\text{-BiPyH}_2]^{2+}$ bipyridine cations are assumed to have a "flat-on" or "edge-on" orientation. Molecules are aligned along the $[10\bar{1}]$ direction. The self-assembly is mainly driven by an electrostatic interaction between protonated bipyridine cations and chlorine anions. **Figure 7h** shows a model for the overlayer growth on top of a surface chloride.

**Figure 8a** shows an STM image of Au surface after prolonged immersion of Au/mica film into the acidic solution of 4,4′-BiPy. A new overlayer with a long-range order was observed as shown in **Figure 8b**. The overlayer consists of bright stripes with a periodicity of ~ 10 Å. A growth of the next top layers can be seen at the left side of **Figure 8c**. The top layer, is rotated in respect to the bottom layer, at an angle of 120°, indicating a three-dimensional growth with the Au(111) surface registry. The stripes of the top layer consist of bright protrusions with a height of 1.5–1.8 Å. A TER spectrum taken on this surface is shown in **Figure 8f**. In-plane vibrational modes are observed above 1000 $cm^{-1}$. Six vibrational peaks are found in the spectrum: peaks at 1606, 1503, 1293, 1225, 1071 and 1017 $cm^{-1}$. The observed vibrational frequencies correspond to protonated form of 4,4′-BiPy [57]. No out-of-plane modes are observed, suggesting the "edge-on" molecular orientation. Below 1000 $cm^{-1}$, only a small peak at ~255 $cm^{-1}$ is observed. Pettinger *et al.* assigned vibration at this frequency to the metal-halogen vibration of a surface complex containing metal adatom, halogen ions and pyridine [58].

An optical microscopic image of the sample after a prolonged immersion into the solution is shown in **Figure 8d**. Rectangular shaped, 3D islands of different sizes are found on the surface. Depression defects are always seen near the islands. We speculate that these defects act as a supply of Au adatoms that are further incorporated into the crystal. **Figure 8f** shows a Raman spectrum taken within the area of a large 3D island using a confocal Raman unit. The spectrum above 1000 $cm^{-1}$ is consistent with the Raman spectrum of a solid $BiPyH_2Cl_2$ [59]. The spectrum is similar to the TER spectrum but bands are more intense.

In contrast to TER spectrum, out-of-plane modes are also observed suggesting that molecules with "flat-on" orientation are also present. A very weak Raman signals were also observed at 2460 and 3450 $cm^{-1}$. They were assigned to the $N\text{-}H^{+}\ldots Cl^{-}$–4,4′-BiPy stretching, and free N-H stretching vibrations, respectively [60, 61]. At very low frequencies, two strong peaks at ~88 and 116 $cm^{-1}$ with the shoulder at 134 $cm^{-1}$ were observed. Similarly, low-frequency Raman peaks are observed

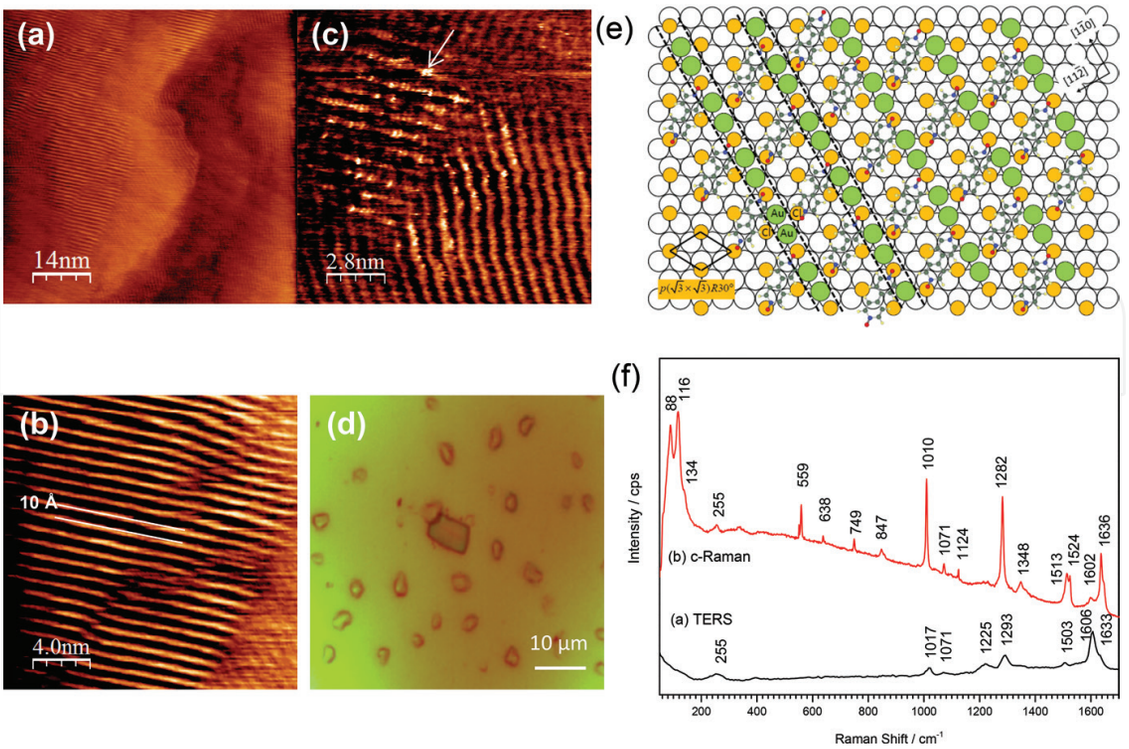


**Figure 8.** STM images after prolonged immersion of an Au slide into 1 mM ethanolic solution of 4,4-BiPy, acidified to pH = 3 with HCl: (a) a 70 × 70 nm image showing a chain structure; (b) a 20 × 20 nm zoomed image of the chain structure; (c) a 14 × 14 nm zoomed image of the chain structure showing development of the next top layers; (d) a bright-field microscope image of the Au slide showing surface-grown large 3D crystals; (e) a possible molecular model of the chain structure and (f) Raman spectra. Adapted from Rzeznicka *et al*. Copyright@Elsevier B.V [55].

in dinuclear Au complexes containing Cl, and in the case of pyridine adsorption on Ag electrodes. In dimethylgold halides, Au-Au vibrations are found at ~74 $cm^{-1}$ [62]. Thus, these two peaks were assigned to Au-Au and Au-Cl stretching vibrations, respectively. The assignment was supported by the results of secondary mass ion spectrometry (SIMS) which yields information on the surface species. A highest intensity gain was observed for $m/z = 465$ corresponding to $Au_2Cl_2$ species [55].

## 5. Future prospects and challenges

In this chapter, we have reviewed the principles of STM-based TERS and discussed how molecular binding and halogen overlayer influence the intensity of the Raman signals. These two effects contribute to CE, which is system specific, that is, its magnitude depends on the metal-molecule system and experimental conditions of sample preparation. Further studies on the effects of molecular orientation on signal enhancement under more well-defined conditions, such as those provided by UHV environment, can bring us more knowledge on the mechanism of TERS.

Combined studies using cryogenic, polarized UHV-TERS and nanolithographically fabricated model nanostructures, supported by the state-of-the-art calculations to determine the Raman polarizability tensor components of a molecule-metal can lead to the formulation of TERS surface selection rules [46, 63, 64]. Home built STM-TERS systems in the Duyene and

the Wang group are making first steps in this direction. We have collaborated with the company Unisoku in Japan in the development of a commercial UHV-TERS and have shown its capability to obtain relatively strong Raman signals from organic molecules adsorbed on a metal surface. Cryogenic cooling has been found to resolve issues of spectral fluctuations, as shown in **Figure 9**.

Fukumura *et al.* have proposed that single molecule sensitivity could be facilitated by employing vibrational excitation of molecules using inelastic scattering of tunneling electrons synchronized with the laser excitation to the excited states [65]. The technical challenge with this approach lies in the synchronization of the laser pulse with the electric pulse. The Duyene group has just started incorporating ultra-short laser pulses with UHV-TERS [66]. Apart from a purely academic interest, STM-TERS could contribute to understanding surface chemistry under ambient or solution conditions and aid in the development of large-scale metal protective organic layers. Moreover, metal leads are also important in electrical applications. It is a challenging task to minimize Ohmic losses for metal electrodes covered with thin organic films. As demonstrated in this chapter, halogen-modified surfaces could act as templates for the subsequent growth of metal-organic framework structures directly on the surfaces of metals.

Studies using electrochemical STM-TERS (EC STM-TERS) could assist in the fabrication of conductive metal/organic molecule thin films by utilizing anion-overlayers as templates for formation of well-defined organic thin films, as demonstrated here. Such organic thin films are increasingly important in the field of sensing, molecular electronics and optoelectronics. A challenge in Raman spectroscopy of organic molecules adsorbed on metal surfaces is detection of low frequency Raman signals, which give information on the chemical state of the molecule and possible metal–organic surface complex formation. Utilizing ultra-narrowband notch filters and a pinhole in front of the spectrograph slit, we recently observed signals down

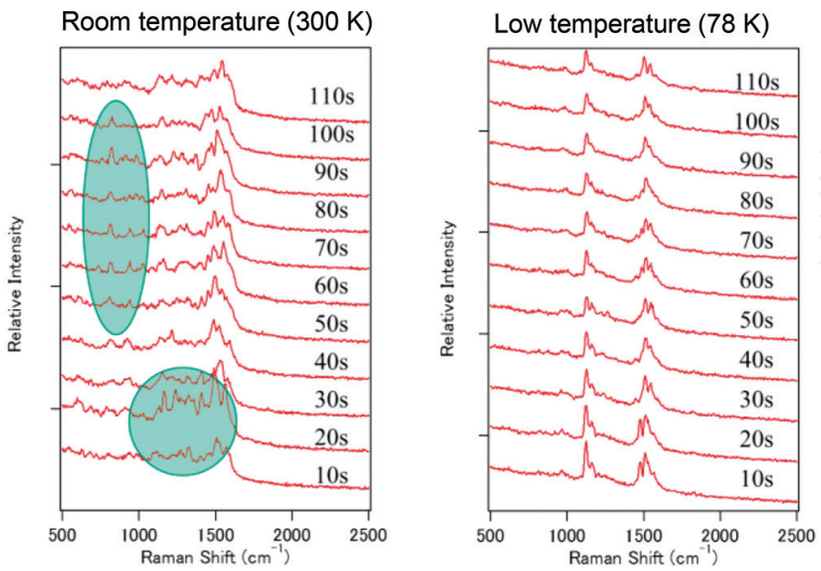


**Figure 9.** UHV-TER spectra of 1, 2-di-(4-pyridyl)-ethylene (BPE) at room (300 K) (left) and liquid nitrogen temperature (78 K)(right). Adapted from http://www.unisoku.com/products.

to 15 $cm^{-1}$. Improvement in the optical density of the filters would allow for detection of Raman signal from organic molecules that have weak Raman scattering cross-sections.

In the field of lithium-ion batteries, growth of conductive metal-organic interfaces with small contact resistances and catalytic functions is very attractive but remains very challenging. New experimental setups based on the TERS idea could allow for the study of interfacial processes during battery operation. A challenge in this case is a strong fluorescence signal from various battery components such as organic electrolytes, additives, binders, and so on. In this respect, systems based on near-infrared excitation would offer elimination of the fluorescence signal. Another advantage of this approach based on hyper Raman phenomena is that Raman signals originate from the small focal volume, which allow for distinguishing the interface signals from the signals originating from the bulk.

In summary, the demand for chemical analysis with nanoscale resolution makes SPM-based TERS attractive in many fields of science and engineering. We expect that, in the next 10 years, we will witness further developments in this technique and obtain more system-specific information, which will expand our knowledge of surface chemistry and the interactions of molecules with light in confined fields. Understanding system-specific chemical enhancement will advance the field of molecular plasmonics, which is an emerging field of science exploiting the molecule-plasmon interactions to harness light at the nanoscale for nanophotonic devices.

## Author details

Izabela Rzeznicka[1]* and Hideyuki Horino[2]

*Address all correspondence to: izabela@shibaura-it.ac.jp

1 Graduate School of Science and Engineering, Shibaura Institute of Technology, Tokyo, Japan

2 Department of Chemistry for Materials, Mie University, Tsu, Japan

## References

[1] Raman CV, Krishnan KS. A theory of the optical and electrical properties of liquids. Proceedings of the Royal Society of London. 1928;**117**:589-599. DOI: 10.1098/rspa.1928.0021

[2] Schrötter HW, Klöckner HW. Raman spectroscopy of gases and liquids. In: Weber A, editors. Topics in Current Physics. 1st ed. Berlin: Springer Berlin Heidelberg; 1979. pp. 123-166. DOI: 10.1007/978-3-642-81279-8_4

[3] Fleischmann M, Hendra PJ, McQuillan AJ. Raman spectra of pyridine adsorbed at a silver electrode. Chemical Physics Letters. 1974;**26**:163-166. DOI: 10.1016/0009-2614(74)85388-1

[4] Albrecht MG, Creighton JA. Anomalously intense Raman spectra of pyridine at a silver electrode. Journal of the American Chemical Society. 1977;**99**:5215-5217. DOI: 10.1021/ja00457a071

[5] Jeanmaire DL, Van Duyne RP. Surface Raman spectroelectrochemistry. Journal of Electroanalytical Chemistry. 1977;**84**:1-20. DOI: 10.1016/S0022-0728(77)80224-6

[6] Otto A. In: Cardona M, Guntherodt G, editors. Light Scattering in Solids IV. Berlin: Springer Berlin Heidelberg; 1984. pp. 289-418. DOI: 10.1007/3-540-11942-6_24

[7] Moskovits M. Surface-enhanced spectroscopy. Reviews of Modern Physics. 1985;**57**:783-826. DOI: 10.1103/RevModPhys.57.783

[8] Campion A, Kambhampati P. Surface-enhanced Raman scattering. Chemical Society Reviews. 1998;**27**:241-250. DOI: 10.1039/a827241z

[9] Schatz GC, Young MA, Van Duyne RP. Electromagnetic mechanism of SERS. In: Katrin K, Martin M, Harald K, editors. Topics in Applied Physics. 1st ed. Berlin: Springer Berlin Heidelberg; 2006. pp. 19-45. DOI: 10.1007/3-540-33567-6_2

[10] Le Ru EC, Etchegoin PG. Principles of Surface-Enhanced Raman Spectroscopy. 1st ed. Amsterdam: Elsevier; 2009. 663 p. DOI: 10.1016/B978-0-444-52779-0.00012-X

[11] Moskovits M. Surface selection rules. The Journal of Chemical Physics. 1982;**77**:4408-4416. DOI: 10.1063/1.444442

[12] Le Ru EC, Etchegoin PG. Quantifying SERS enhancements. MRS Bulletin. 2013;**38**:631-640. DOI: 10.1557/mrs.2013.158

[13] Morton SM, Jensen L. Understanding the molecule–surface chemical coupling in SERS. Journal of the American Chemical Society. 2009;**131**:4090-4098. DOI: 10.1021/ja809143c

[14] Vivoni A, Birke RL, Foucault R, Lombardi JR. Ab Initio frequency calculations of pyridine adsorbed on an adatom model of a SERS active site of a silver surface. The Journal of Physical Chemistry. B. 2003;**107**:5547-5557. DOI: 10.1021/jp027642o

[15] Cardini G, Muniz-Miranda M. Density functional study on the adsorption of pyrazole onto silver colloidal particles. The Journal of Physical Chemistry. B. 2002;**106**:6875-6880. DOI: 10.1021/jp014205l

[16] Johansson P. Illustrative direct ab initio calculations of surface Raman spectra. Physical Chemistry Chemical Physics. 2005;**7**:475-482. DOI: 10.1039/b415535a

[17] Lombardi JR, Birke RL, Lu T, Xu J. Charge transfer theory of surface enhanced Raman spectroscopy: Herzberg–Teller contributions. The Journal of Chemical Physics. 1986;**84**:4174-4180. DOI: 10.1063/1.450037

[18] Lombardi JR, Birke RL. A unified approach to surface-enhanced Raman spectroscopy. Journal of Physical Chemistry C. 2008;**112**:5605-5617. DOI: 10.1021/jp800167v

[19] Wu D-Y, Ren B, Jiang Y-X, Xu X, Tian Z-Q. Density functional study and normal-mode analysis of the bindings and vibrational frequency shifts of the pyridine–M (M = Cu, Ag, Au, Cu+, Ag+, Au+, and Pt) complexes. The Journal of Physical Chemistry. A. 2002;**106**:9042-9052. DOI: 10.1021/jp025970i

[20] Futamata M. Adsorbed state of 4,4′-BiPy and BiPyH22+ on Au(111) electrode. The Journal of Physical Chemistry B. 2001;**105**:6933-6942. DOI: 10.1021/jp010344r

[21] Stöckle RM, Suh YD, Deckert V, Zenobi R. Nanoscale chemical analysis by tip-enhanced Raman spectroscopy. Chemical Physics Letters. 2000;**318**:131-136. DOI: 10.1016/S0009-2614(99)01451-7

[22] Hayazawa N, Inouye Y, Sekkat Z, Kawata S. Metallized tip amplification of near-field Raman scattering. Optics Communication. 2000;**183**:333-336. DOI 10.1016/S0030-4018(00)00894-4

[23] Binnig G, Rohrer H, Gerber C, Weibel E. Surface studies by scanning tunneling microscopy. Physical Review Letters. 1982;**49**:57-61. DOI: 10.1103/PhysRevLett.49.57

[24] Scanning tunneling microscopy I. In: Wiesendanger R, Gntherodt HJ, editors. Surface Sciences. Berlin: Springer-Verlag Berlin Heidelberg; 1992

[25] Jaklevic RC, Lambe J. Molecular vibration spectra by electron tunneling. Physical Review Letters. 1966;**17**:1139-1140. DOI: 10.1103/PhysRevLett.17.1139

[26] Dionne JA, Atwater HA. Plasmonics: Metal-worthy methods and materials in nanophotonics. MRS Bulletin. 2012;**37**:717-724. DOI: 10.1557/mrs.2012.171

[27] Raman Microscopy: Development and Applications. London: Academic Press Limited; 1996. 463 p

[28] Novotny L, Bian RX, Xie XS. Theory of nanometric optical tweezers. Physical Review Letters. 1997;**79**:645-648. DOI: 10.1103/PhysRevLett.79.645

[29] Pettinger B, Ren B, Picardi G, Schuster R, Ertl G. Nanoscale probing of adsorbed species by Tip-enhanced Raman spectroscopy. Physical Review Letters. 2004;**92**:096101. DOI: 10.1103/PhysRevLett.92.096101

[30] Steidtner J, Pettinger B. Tip-enhanced Raman spectroscopy and microscopy on single dye molecules with 15A nm resolution. Physical Review Letters. 2008;**100**:23610101. DOI: 10.1103/PhysRevLett.100.236101

[31] Schmid T, Yeo BS, Zhang W, Zenobi R. Tip enhancement. In: Kawata S, Shalaev VM, editors. Amsterdam: Elsevier; 2007. p.115-155. DOI: 10.1016/B978-044452058-6/50005-0

[32] Ren B, Picardi G, Pettinger B. Preparation of gold tips suitable for tip-enhanced Raman spectroscopy and light emission by electrochemical etching. The Review of Scientific Instruments. 2004;**75**:837-841. DOI: 10.1063/1.1688442

[33] Williams C, Roy D. Fabrication of gold tips suitable for tip-enhanced Raman spectroscopy. Journal of vacuum science & technology. B, Microelectronics and nanometer structures. 2008;**26**:1761-1764. DOI: 10.1116/1.2981078

[34] Wang X, Huang S-C, Huang T-X, Su H-S, Zhong J-H, Zeng Z-C, Li M-H, Ren B. Tip-enhanced Raman spectroscopy for surfaces and interfaces. Chemical Society Reviews. 2017;**46**:4020-4041. DOI: 10.1039/C7CS00206H

[35] Deckert-Gaudig T, Richter M, Knebel D, Jähnke T, Jankowski T, Stock E, Deckert V. A modified transmission tip-enhanced Raman scattering (TERS) setup provides access to opaque samples. Applied Spectroscopy. 2014;**68**:916-919. 10.1366/13-07419

[36] Aravind P, Metiu H. The effects of the interaction between resonances in the electromagnetic response of a sphere-plane structure; applications to surface enhanced spectroscopy. Surface Science. 1983;**124**:506-528. DOI: 10.1016/0039-6028(83)90806-3

[37] Nordlander P, Oubre C, Prodan E, Li K, Stockman MI. Plasmon hybridization in nanoparticle dimers. Nano Letters. 2004;**4**:899-903. DOI: 10.1021/nl049681c

[38] Downes A, Salter D, Elfick A. Finite element simulations of tip-enhanced Raman and fluorescence spectroscopy. The Journal of Physical Chemistry B. 2006;**110**:6692-6698. DOI: 10.1021/jp060173w

[39] Hartschuh A. Tip-enhanced near-field optical microscopy. Angewandte Chemie, International Edition, 2008;**47**:8178-8191. DOI: 10.1002/anie.200801605

[40] Notingher I, Elfick A. Effect of sample and substrate electric properties on the electric field enhancement at the apex of SPM nanotips. The Journal of Physical Chemistry B. 2005;**109**:15699-15706. DOI: 10.1021/jp0523120

[41] Pettinger B, Domke KF, Zhang D, Schuster R, Ertl G. Direct monitoring of plasmon resonances in a tip-surface gap of varying width. Physical Review B. 2007;**76**:113409. DOI: 10.1103/PhysRevB.76.113409

[42] Pettinger B, Ren B, Picardi G, Schuster R, Ertl G. Tip-enhanced Raman spectroscopy (TERS) of malachite green isothiocyanate at Au(111): bleaching behavior under the influence of high electromagnetic fields. Journal of Raman Specroscopy. 2005;**36**:541-550. DOI: 10.1002/jrs.1332

[43] Ren B, Picardi G, Pettinger B, Schuster R, Ertl G. Tip-enhanced Raman spectroscopy of benzenethiol adsorbed on Au and Pt single-crystal surfaces. Angewandte Chemie, International Edition. 2005;**44**:139-142. DOI: 10.1002/anie.200460656

[44] Fang Y, Zhang Z, Chen L, Sun M. Near field plasmonic gradient effects on high vacuum tip-enhanced Raman spectroscopy. Physical Chemistry Chemical Physics. 2015;**17**:783-794. DOI: 10.1039/c4cp03871a

[45] Golovin A, Polubotko A. Analysis of peculiarities of the SEHRS and SERS spectra of 4, 4′-Bipyridine molecule on the base of the dipole-quadrupole theory. Chemical Physics Letters. 2016;**662**:208-213. DOI: 10.1016/j.cplett.2016.09.047

[46] Zhang R, Zhang Y, Dong ZC, Jiang S, Zhang C, Chen LG, Zhang L, Liao Y, Aizpurua J, Luo Y, Yang JL, Hou JG. Chemical mapping of a single molecule by plasmon-enhanced Raman scattering. Nature. 2013;**498**:82-86. DOI: 10.1038/nature12151

[47] Duan S, Tian G, Luo Y. Visualization of vibrational modes in real space by tip-enhanced non-resonant Raman spectroscopy. Angewandte Chemie, International Edition. 2016; **55**:1041-1045. DOI: 10.1002/anie.201508218

[48] Benz F, Schmidt MK, Dreismann A, Chikkaraddy R, Zhang Y, Demetriadou A, Carnegie C, Ohadi H, de Nijs B, Esteban R, Aizpurua J, Baumberg JJ. Single-molecule optomechanics in "picocavities". Science. 2016;**354**:726-729. DOI: 10.1126/science.aah5243

[49] Zhang C, Chen B-Q, Li Z-Y. Optical origin of subnanometer resolution in tip-enhanced Raman mapping. Journal of Physical Chemistry C. 2015;**119**:11858-11871. DOI: 10.1021/acs.jpcc.5b02653

[50] Hoffmann FM. Infrared reflection-absorption spectroscopy of adsorbed molecules. Surface Science Reports. 1983;**3**:107109-107192. DOI: 10.1016/0167-5729(83)90001-8

[51] Le Ru E, Meyer S, Artur C, Etchegoin P, Grand J, Lang P, Maurel F. Experimental demonstration of surface selection rules for SERS on flat metallic surfaces. Chemical Communications. 2011;**47**:3903-3905. DOI: 10.1039/C1CC10484E

[52] Rzeźnicka II, Horino H, Kikkawa N, Sakaguchi S, Morita A, Takahashi S, Komeda T, Fukumura H, Yamada T, Kawai M. Tip-enhanced Raman spectroscopy of 4,4′-bipyridine and 4,4′-bipyridine N,N′-dioxide adsorbed on gold thin films. Surface Science. 2013;**617**:1-9. DOI: 10.1016/j.susc.2013.08.010

[53] M. J. Frisch et al., Gaussian 09, Gaussian, Inc., Wallingford CT In 2010

[54] Atkins PW, Friedman RS. Molecular Quantum Mechanics. 5th ed. Oxford: Oxford Univ. Press; 2010. 573 p

[55] Rzeźnicka I, Horino H, Yagyu K, Suzuki T, Kajimoto S, Fukumura H. Chlorine adlayer-templated growth of a hybrid inorganic–organic layered structure on Au (111). Surface Science. 2016;**652**:46-50. DOI: 10.1016/j.susc.2016.03.007

[56] Gao W, Baker TA, Zhou L, Pinnaduwage DS, Kaxiras E, Friend CM. Chlorine adsorption on Au(111): chlorine overlayer or surface chloride? Journal of the American Chemical Society. 2008;**130**:3560-3565. DOI: 10.1021/ja077989a

[57] Pérez-Jiménez AJ, Sancho-García JC, Pérez-Jordá JM. Torsional potential of 4,4′-bipyridine. Ab initio analysis of dispersion and vibrational effects. Journal of Chemical Physics. 2005;**123**:134309. DOI: org/10.1063/1.2043107

[58] Pettinger B, Wtzel H. Surface enhanced raman spectroscopy of pyridine on Ag electrodes. Surface complex formation. Chemical Physics Letters. 1981;**78**:398-403. DOI: 10.1016/0009-2614(81)80041-3

[59] Diao Y-X, Han M-J, Wan L-J, Itaya K, Uchida T, Miyake H, Yamakata A, Osawa M. Adsorbed structures of 4,4′-bipyridine on Cu(111) in acid studied by STM and IR. Langmuir. 2006;**22**:3640-3646. DOI: 10.1021/la052765w

[60] Huong PV, Schlaak M. Raman and infrared band shapes of the N-H+...X-hydrogen bond in trimethylaminium halide crystals. Chemical Physics Letters. 1974;**27**:111-113. DOI: 10.1016/0009-2614(74)80456-2

[61] Foglizzo R, Novak A. Low frequency infrared and Raman spectra of hydrogen bonded pyridinium halides. The Journal of Chemical Physics. 1969;**50**:5366-5373. DOI: 10.1063/1.1671056

[62] Bessonov AA, Basova TV, Kiselev VG, Sheludyakova LA, Morozova NB, Igumenov IK. Vibrational interactions in dimethylgold(III) halides and carboxylates. Vibrational Spectroscopy. 2009;**51**:283-288. DOI: 10.1016/j.vibspec.2009.07.003

[63] Jiang N, Foley ET, Klingsporn JM, Sonntag MD, Valley NA, Dieringer JA, Seideman T, Schatz GC, Hersam MC, Van Duyne RP. Observation of multiple vibrational modes in ultrahigh vacuum tip-enhanced Raman spectroscopy combined with molecular-resolution scanning tunneling microscopy. Nano Letters. 2012;**12**:5061-5067. DOI: 10.1021/nl2039925

[64] Nagasawa F, Takase M, Nabika H, Murakoshi K. Polarization characteristics of surface-enhanced Raman scattering from a small number of molecules at the gap of a metal nano-dimer. Chemical Communications. 2011;**47**:4514-4516

[65] Fukumura H, Irie M, Iwasawa Y, Masuhara H, Uosaki K, editors. Molecular Nano Dynamics. 1st ed. Verlag: John Wiley & Sons; 2009. 314 p

[66] Pozzi EA, Sonntag MD, Jiang N, Chiang N, Seideman T, Hersam MC, Van Duyne RP. Ultrahigh vacuum tip-enhanced Raman spectroscopy with picosecond excitation. Journal of Physical Chemistry Letters. 2014;**5**:2657-2661. DOI: 10.1021/jz501239z

IntechOpen